ISSN (Print) 1226-1750
ISSN (Online) 2233-6656
Journal of Magnetics 30(4), 544-552 (2025) https://doi.org/10.4283/JMAG.2025.30.4.544

Morphological, Structural, Electrical and Magnetic Properties of Ni Thin Films Deposited on Si Substrates

T. Kacel[1]*, A. Guittoum[2], M. Hemmous[2], R. M. Öksüzoglu[3], and A. Azizi[4]

[1]*Research Center in Industrial Technologies (CRTI) P.O. Box 64, Cheraga 16014 Algiers, Algeria*
[2]*Nuclear Research Centre of Algiers, 02 Bd Frantz Fanon, BP 399 Alger-Gare, Algiers, Algeria*
[3]*Department of Materials Science and Engineering, Faculty of Engineering, Anadolu University, Eskişehir 26470, Turkey*
[4]*Laboratory of Chemistry, Molecular Engineering and Nanostructures, Chemistry Department, University of Ferhat Abbas Setif-1, 19000 Setif, Algeria*

(Received 10 January 2025, Received in final form 7 November 2025, Accepted 14 November 2025)

In this investigation, Ni thin films have been deposited by pulsed electrodeposition (PED) method onto *n*-Si (111) substrate using different applied potentials ranging from -2.6 to -1.6 V. As a result, the effect of Ni thickness manipulated by the applied potential on the structural, electrical, morphological, and magnetic properties of Ni film is investigated. According to the RBS (Rutherford Backscattering Spectrometry), the film thickness increases from 50 to 390 nm as the applied voltage decreases. The XRD (X-ray Diffraction) results reveals that the films are of polycrystalline growth with the <111> texture. Besides, all the films show a negative out-in-plane strain and have a critical value (V_{cr}) of the applied potential of -2.2 V corresponding to the absolute maximum strain value. Moreover, the average grain size improves proportionally with the film thickness. AFM (Atomic Force Microscopy) shows that the uniform growth of well-distributed three-dimensional islands is achieved by applying -2.2 V. Regarding the electrical properties, Ni film deposited with V_{cr} is characterized by the lower electrical resistivity. The coercive field and the squareness factor steadily improve up to V_{cr}. In contrast, the parallel saturation field rapidly decreases before reaching V_{cr}, then continues to decrease gradually beyond this point. All the above results will be discussed and correlated.

Keywords : applied potential, thickness, Ni thin films, electrodeposition, magnetization curves, coercivity

1. Introduction

Recently, ferromagnetic thin films have attracted significant attention due to their various applications in modern technological devices, including data storage devices, magnetic recording media, sensors, and others [1-5]. The structural and magnetic properties of thin film are excellent compared to those of bulk. In general, various methods for preparing ferromagnetic films with good structural and soft magnetic properties have been reported in the literature, such as thermal evaporation, sputtering, molecular beam epitaxy, PECVD, and electrodeposition which are among the most widespread in recent years [6-11]. In particular, the electrodeposition method has numerous advantages, including flexibility, low temperature, low cost and high-quality films compared to other methods [12-15]. In addition, the latter has been adopted to study the different phenomena, such as the corrosion [16, 17], the electrical [18], the mechanical [19], the oxidation [20] and the magnetic behavior [21, 22]. On the other hand, the morphology, structural, electrical and magnetic properties of the ferromagnetic film deposited by this method are highly-sensitive to the variation of the operating conditions, such as the electrolyte bath, pH, additives, and applied potential [23-28]. Basically, the potential is the fine condition that can attract extensive attention due to their influence on the surface morphology and structure of the films. In turn, these latter ones are highly essential factors adopting to control the magnetic behaviors of the ferromagnetic films. In fact, several researchers have been reported in literature focusing on the study of the correlation between the structural and magnetic properties [29-32]. Moreover, experimentally, the thickness, stress and grain size can affect the magnetic properties and modify their magnetic behavior such as the coercivity, the magnetization and the

*Corresponding author: Tel: +213-23-14-14-47
e-mail: t.kacel@crti.dz

magnetic anisotropy constants [33-35].

In this study, we have examined the effect of the applied potential (ranging from -2.6 to -1.6 V) and the Ni thickness (in the 50-390 nm range) on the structural, electrical and magnetic properties of Ni thin films elaborated by pulsed electrodeposition on Si substrate. Rutherford backscattering spectrometry (RBS) and grazing incidence X-ray diffraction (GIXRD) were carried out to measure the Ni thicknesses and to obtain the structural parameters such as the preferential orientation, the out-in-plane strain ε^{hkl}(%), and the average grain size <D (nm)>. Atomic force microscopy (AFM) was used to study the morphology of the Ni films. The electrical properties of the samples were investigated by the four-point probe technique (M4PP). The magnetic parameters were extracted from the hysteresis curves with the means of the vibrating sample magnetometer (VSM). The variation of these parameters was studied and discussed as a function of the applied potential and the Ni thickness. A summary and a conclusion are given.

2. Experimental Details

In this experimental work, pulsed electrodeposition (PED) is used to elaborate Ni thin films on *n*-Si (111) substrates at various applied potentials (-2.6, -2.4, -2.2, -1.8 and -1.6 V). Electrodeposition of Ni films was carried out using 0.5 M of Nickel sulfate hexahydrate ($NiSO_4 \cdot 6H_2O$), 0.4 M of boric acid (H_3BO_3) and saccharin dissolved in deionized water at room temperature. The mixed solution was loaded into a three-electrode Teflon cell connected to a computer-controlled potentiostat/galvanostat (VMP3) with EC-Lab express software. Note that *n*-Si substrate as the cathode, a platinum plate as the counter electrode and an Ag/AgCl (sat) as the standard electrode. The deposition time and the pH of the solution were fixed to 30 s and 3, respectively.

In this experimental study, the following characterization techniques were used: (i) the Rutherford backscattering spectrometry (RBS) using 2 MeV He^+ ions (α particles) delivered by a 3.75 MV Van de Graaf accelerator, (ii) the grazing incidence X-ray diffraction (GIXRD) working in the θ-θ mode with wavelength λ_{Cu}= 1.54056 Å as incident radiation at grazing angle of 1,and the diffraction angle 2θ ranging from 40° to 100° with a step size of 0.02°, (iii) the atomic force microscopy (AFM) was used to follow the surface morphology and the roughness, (iv) the four point probe (M4PP) for measure the sheet resistance and electrical resistivity of the samples, and (v) the vibrating sample magnetometer (VSM) to study the magnetic parameters applying an external magnetic field in parallel and perpendicular to the samples surface.

3. Results and Discussions

3.1. Structural properties

3.1.1. Rutherford backscattering spectrometry RBS

It is well known that the thickness has a significant impact on the physiochemical properties of thin films. In this regard, the Ni film thickness has been manipulated by varying the applied potential from -2.6 to -1.6 V during the deposition process. Regarding the direct correlation between the applied potential and the film thickness, RBS experiments were conducted to measure the film thickness and probe the substrate-film interface. By way of example, Fig. 1(a) illustrates the RBS spectra corresponding to the lowest applied potential (-2.6 V) simulated (solid lines) using the RUMP code [36]. There is no interdiffusion at the materials interface, as evidenced by the fact that the contribution signals of the Ni and Si elements are clearly separated by a very low yield range. Additionally, for all samples, there are no peaks that can be attributed to contaminants. The Ni thicknesses measured

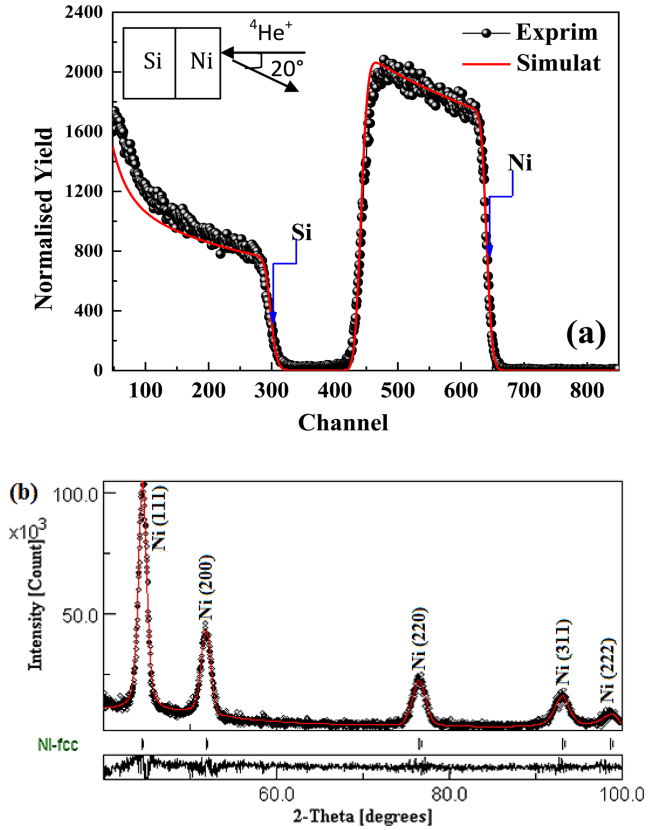

Fig. 1. (Color online) (a) Example of *RBS* spectra and (b) example of *XRD* diffraction spectra for -2.6 V applied potential (thicker film).

Table 1. Ni thicknesses t, Texture coefficient $T_{C(hkl)}$, out-of-plane strain ε (%), root-mean-square rms(nm), square resistance R_L and electrical resistivity ρ for different applied potential.

Potential (V)	Thickness t (nm)	Texture coefficient $T_{C(hkl)}$					ε (%)	RMS (nm)	R_L (Ω/□)	ρ (μΩ.cm)
		$T_{C(111)}$	$T_{C(200)}$	$T_{C(220)}$	$T_{C(311)}$	$T_{C(222)}$				
-2.6	390	1.26	1.13	1.16	0.71	0.74	-0.15	10.77	0.31	12.09
-2.4	320	1.34	1.16	1.04	0.71	0.75	-0.32	16.25	0.41	13.12
-2.2	254	1.31	1.11	1.11	0.73	0.75	-0.38	12.91	0.45	11.43
-1.8	120	1.40	1.25	1.03	0.73	0.59	-0.14	11.97	1.42	17.04
-1.6	50	1.41	1.17	0.96	0.68	0.78	- 0.15	04.32	2.44	12.2

are equal to 390, 320, 254, 120 and 50 nm corresponding to -2.6, -2.4, -2.2, -1.8, and -1.6 V, respectively. As a result, the impact of the applied potential on the Ni thickness is evident as the Ni film thickness decreases linearly with increasing applied potential from -2.6 to -1.6 V (see Table 1).

3.1.2. X-Ray Diffraction XRD

To investigate the structural evolution of the Ni film as a function of applied potential (i.e., Ni thickness), grazing incidence X-ray diffraction (GIXRD) experiment was carried out on all samples. Deriving the main structural parameter (texture, out-in-plane strain, and mean grain size) through the full-profile refinement of the XRD patterns using the MAUD software based on the Rietveld method [37], helps to provide a deep insight into the structural properties of the Ni films. Example of GIXRD patterns of the Ni films for the lowest applied potential (thicker film) is shown in Fig. 1(b). When comparing with JCPDS Card Ref. code. 004-0850 of the Ni [38], five diffraction peaks were observed for the same diffraction angle range 2θ (40°-100°). The five peaks have been identified as diffraction planes (111), (200), (220), (311) and (222) of the face-centered cubic (fcc) structure of the Ni phase. In fact, no impurity phases were detected within the X-ray diffractometer's detection limit, confirming the RBS results, i.e., the elaboration of high-purity Ni thin films. In a polycrystalline material, the grains grow along preferred orientations, creating a crystallographic texture. The latter has a considerable impact on the properties and performance of the elaborate thin films.

In our study, the texture coefficients $TC_{(hkl)}$ of the *hkl* plane were compared in order to determine the pre-ferential orientation of the Ni films. For each orientation, the texture coefficient is determined as [39]:

$$TC_{(hkl)} = \frac{I_{(hkl)}/I_{o(hkl)}}{(1/N)[\Sigma_N I_{(hkl)}/I_{o(hkl)}]} \quad (1)$$

Where $I_{(hkl)}$ is the measured intensity, $I_{0(hkl)}$ is the relative intensity of the corresponding plane given in ref. [38], and *N* is the number of reflections.

The texture coefficient values of the diffraction planes for all samples are presented in Table 1. It is clear that the (111) diffraction plane exhibits the highest values of *TC* for all samples (ranging from 1.26 to 1.41) in comparison to the other ones, i.e., the highest *TC* values of the {200}, {220}, {311} and {222} planes are all consistently lower than the lowest $TC_{(111)}$values, indicating that the majority of grains grow in the <111> direction. The high $TC_{(hkl)}$ values of the (111) plane might be proof that the Ni films grow with the <111> texture on all samples. This result is well-aligned with our earlier research [40]. We believe that all the samples growth following the direction parallel to the plane of Si (111) substrate. It is commonly known that in a face-centered cubic (fcc) material, the film's (111) plane has the lowest surface energy [41]. On the other hand, the surface atomic density of Ni (111) is higher than the other ones; the Ni (111) surface may play a role of low barriers for surface self-diffusion [30].

The variation of the lattice parameter, *a* (*Å*), as a function of applied potential goes through two stages (see Fig. 2(a)); in the first, as the potential is increased up to a critical potential V_{Cr} (-2.2 V), the lattice parameter monotonically decreases to a minimum value equal to 3.5108 Å. In the second, or beyond the critical potential, the value of *a* (*Å*) increases up to -1.8 V and then nearly stays constant as the applied potential increases once again. In order to determine the state of the strain, we calculated the out-in-plane strain using the measured a_{meas} and bulk a_{bulk} lattice parameter values, which is defined as [42]:

$$\varepsilon^{hkl} = (a_{meas} - a_{bulk})/a_{bulk} \quad (2)$$

The strain has been calculated for all samples. Table 1 displays the strain values as a function of applied potential and Ni thickness. First, we observe that the strain values are negative, suggesting that the films are under compressive stress. Second, we observe that the

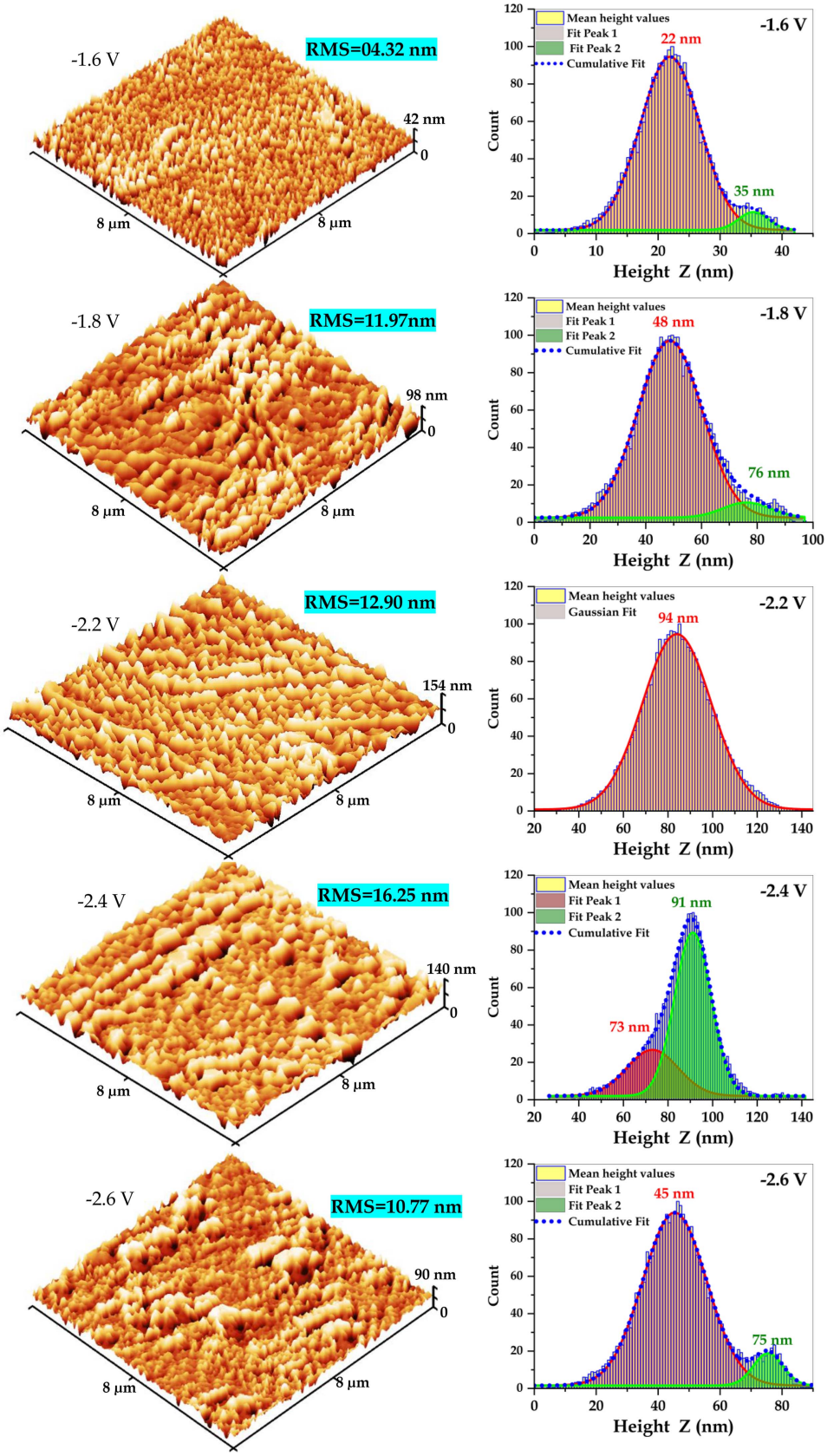

Fig. 2. (Color online) Variation of: (a) lattice parameter *a* (*Å*) vs. applied potential and (b) strain and grain size *D* vs. applied potential.

strain absolute value progressively increases up to V_{Cr} (-2.2 V), then decreases beyond V_{Cr} and finally nearly stays constant as the applied potential is increased further. On the other hand, it is evident that the stress is relieved as the thickness goes beyond 254 nm of Ni thickness which corresponds to the critical applied potential (V_{Cr}).

Fig. 2(b) illustrates the influence of the applied potential on the mean grain size, <D (nm)>, deduced from the Rietveld refinement. It is seen that D decreases when the applied potential increases up to -2.4 V, then D remains constant up to V_{Cr} and above this potential, D linearly decreases even further as the applied potential increases further. In this study, the impact of the applied potential is noticeable: the increase of the applied potential seems to induce a monotonous decrease of Ni thickness, t, which has a proportional effect on the grain size; when t increases, D increases.

3.1.3. Atomic Force Microscopy AFM

As mentioned above, varying the applied potential influences directly the surface morphology of the Ni films, and thus, the electrical and magnetic properties are affected. In this respect, Figs. 3 display the 3D topographic AFM-images of the Ni films deposited at different applied potentials (-1.6, -1.8, -2.2, -2.4, and -2.6 V), similarly recorded in a scan area of (8×8 µm) with a scan rate of 2.00 Hz. Besides, the RMS (Root-Mean-Square) surface roughness and histograms regarding the mean height distribution of different surfaces are presented in the same figure. Note that the AFM-images processing, RMS calculation, and height histograms were carried out using Gwyddion- data analysis software. The

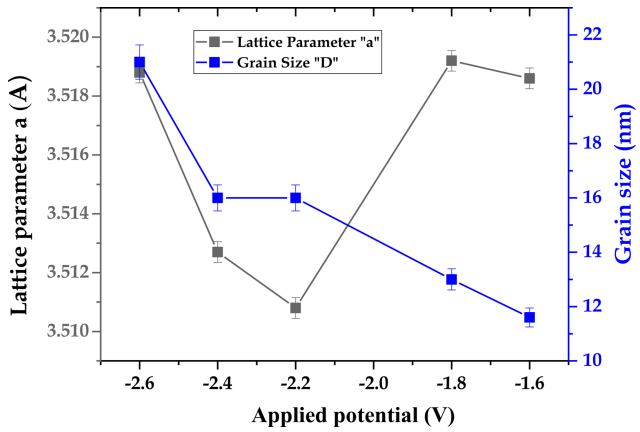

Fig. 3. (Color online) 3D topographic AFM images, Sa (mean roughness), and histograms of median height distribution submitted to the Gaussian deconvolution, corresponding to different applied potentials (-1.6, -1.8, -2.2, -2.4, and -2.6 V) for Ni thin film deposition.

histograms were fitted using Gaussian deconvolution. With the high applied potential (-1.6 V), the beginning of irregular growth of three-dimensional islands can be observed on the surface. By contrast, the growth is most evident by decreasing the applied potential up to -2.6 V. What is interesting is that only with a potential of -2.2 V, a uniform distribution of linear island chains in different directions along the surface appears. Beyond -2.2 V, the grown islands show a high tendency to cluster to form large ones. From a quantitative perspective, the sample prepared at -1.6 V exhibits a homogeneous surface characterized by uniformly distributed islands with an average height of 24 nm. A low density of taller islands, averaging 35 nm, is also present. At -1.8 V, the surface becomes inhomogeneous: the density of shorter islands (≈48 nm) decreases in favor of taller ones (≈76 nm). At the critical potential (V_{Cr} = -2.2 V), the surface becomes highly homogeneous and densely covered with uniformly sized islands averaging 94 nm in height. However, when the deposition potential is further increased to -2.4 V, the surface again becomes inhomogeneous, with a higher density of taller islands (91 nm) compared to shorter ones (73 nm). This trend contrasts with that observed at lower deposition potentials, although the surface remains globally inhomogeneous. Meanwhile, RMS steadily improves with the applied potential from 04.32 nm for -1.6 V to 16.25 nm for -2.4 V and then diminishes beyond. The latter can be attributed to the 2D growth of grains (i.e, horizontal aggregation) that occurred with the low potential (-2.6 V). On the other hand, the Gaussian deconvolution of height histograms reveals the existence of two peaks for all samples except for -2.2 V, reflecting the presence of two kinds of height distribution. The latter indicates a homogeneous islands distribution shown only with the -2.2 V sample, centered around the lowest height (94 nm) compared to the other samples. Note that the RMS roughness increases proportionally with the mean value of height distribution. Based on the above, the uniform growth of well-distributed three-dimensional islands can be achieved by applying an electrodeposition potential at around -2.2 V.

3.2. Electrical properties

The variation of the sheet resistance $R_L(\Omega)=\rho/t$ and the electrical resistivity ρ (µΩ·cm) with applied potential for all sample sis shown in Table 1. We observe that R_L monotonously decreases with increasing applied potential. We believe that the decrease of R_L is due to the increase of film thickness; this behavior indicates that diffusion of conduction electrons at the surface is probably the major contribution to the sheet resistance R_L. Note that the lower

potential (thicker film) is characterized by a smoother surface (as pointed out before in the AFM part, Sect. A. 3) which induced to lower conduction of electrons at the surface. On other hand, R_L decreases with increasing grain size D. It can be said here that even diffusion at the grain boundaries contributes to the decrease of the sheet resistance. In same Table, the electrical resistivity ρ values are between 11.43 and 17.04 μΩ.cm. It should be noted that the lowest electrical resistivity value corresponds to the film deposited by V_{Cr}. On the other hand, we can see clearly that the evolution of electrical resistivity with an increasing of root-mean-square *rms* shows two behaviors, i.e., ρ monotonously decreases simultaneously increasing root-mean-square up to *rms* equal to 12.91 nm (which corresponds to V_{Cr}), then increases as the *rms* is increased further. Moreover, we note that all the films exhibit higher resistivity than of the Ni bulk (ρ_{bulk} = 6.8 μΩ.cm [43]). For the applied potentials -1.8, -2.4 and -2.6 V, we see a monotonous decrease of ρ with thickness t and grain size D.

3.3. Magnetic properties

Hysteresis curves, normalized magnetization M/Ms vs. applied magnetic field H, have been obtained with the vibrating sample magnetometer for two configurations [(a) H in the film plane and (b) H perpendicular to the film plane]. Examples of hysteresis curves are shown in Fig. 4 for the applied potential equal to -2.2 V (V_{Cr}). From the shape of the hysteresis curves, one can infer that all samples are characterized by a magnetic anisotropy in the plane of the film. The magnetic parameters of the films obtained indicated the strong influence of the applied potential on the magnetic behavior of the samples.

3.3.1. The coercive field

The variation of the coercive field, H_C, as a function of the applied potential, for both configurations is shown in Fig. 5. For the parallel configuration, the coercive field, $H_{C//}$, increases slightly with increasing applied potential up to V_{Cr}(-2.2 V), beyond this potential, $H_{C//}$ monotonously decreases from 23 Oe to 13 Oe when the applied potential increases from V_{Cr} to -1.6 V. While for the other configuration, the perpendicular coercive field, $H_{C\perp}$ has three behaviors; $H_{C\perp}$ increases up to -2.4 V, then remains constant (~18.7 Oe) from -1.8 to -2.4 V and beyond this latter potential, $H_{C\perp}$ is increases again. We can see $H_{C\perp}$ progressively decreases with increasing mean grain size $D(nm)$ for all samples. The same behavior was found for the parallel coercive field in the potentials range less than V_{Cr}, beyond this critical potential, $H_{C//}$ is decreased. It is necessary to note that stress factor may play an important role in the behavior of the magnetic parameters. Indeed, a clear correlation between the behavior of $H_{C//}$ and ε_{hkl}(%) was observed; $H_{C//}$ (ε_{hkl}(%)) progressively increases (decreases) with increasing applied potential up to V_{Cr}, beyond the critical potential, stress is relieved (i.e., relaxation) and $H_{C//}$ decreases. We believe that the increasing of H_C with the applied potential (for $V < V_{Cr}$), hence with decreasing Ni thickness, is probably due to the many of pinning centers for magnetic domain walls in the film surface. While, for $V > V_{Cr}$, the decrease of H_C is due to the enhancement of magnetic dipole interactions that results in decreasing the coercive force [44]. This decrease may follow the expected Neel's relation $H_C = At^{-n}$ (t is the film thickness) [45]. On the other hand, the behavior of H_C with the mean grain size D (the increase of H_C with increasing D) makes it possible to say that our

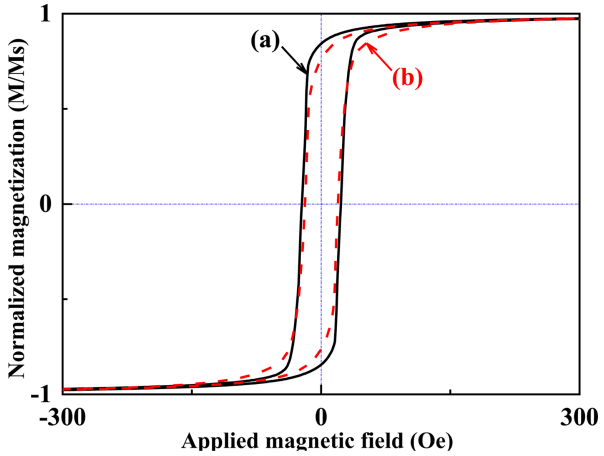

Fig. 4. (Color online) Examples of hysteresis curves for -2.2 V applied potential in two configurations [(a) H in the film plane and (b) H perpendicular to the film plane.

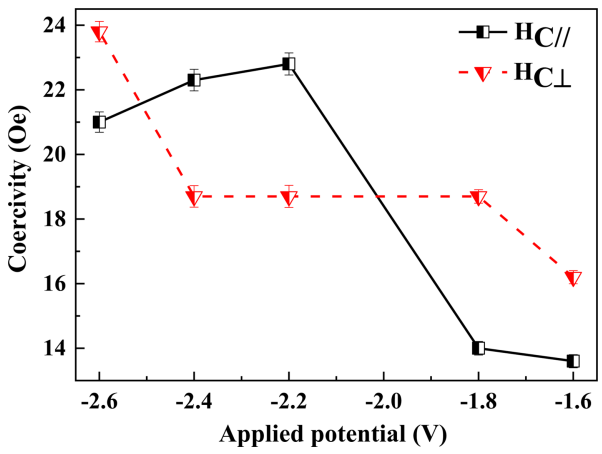

Fig. 5. (Color online) Variation of the coercive field H_C vs. applied potential for H parallel and perpendicular to the film plane.

results follow the Hoffmann's theory which proposes a proportional relation between H_C and D [46]. However, the decrease of H_C with increasing D (for $H_{C//}$, when the applied potential is lower than V_{Cr}, more precisely, when the grain size D is above 16 nm.) indicates that pinning at the grain boundaries seems to be the major contribution to coercivity. Indeed, probably this decrease is due to the variation of Nano crystallite's volume associated with the shape anisotropy [30]. It is well known that the coercivity of an assembly consisting of magnetic particles increases while its size decreases until it reaches a maximum value at a critical size, and then it decreases to zero in the super paramagnetic area [47, 48].

3.3.2. The squareness factor S

The squareness factor allows us to obtain information on the remnant state of a magnetic material and the mechanisms of the magnetization reversal. In Fig. 6, we show the variation of the squareness factor S as a function of the applied potential, for both configurations. It is necessary to note that, for comparison, all squareness factor values are lower than the polycrystalline bulk Ni material, S is equal to 0.866 [49]. On the other hand, we can see clearly the effect of the applied potential on the squareness factor, and also the presence of a critical applied potential, V_{Cr}. The parallel squareness factor $S_{//}$ monotonically increases with increasing applied potential up to V_{Cr}, then, $S_{//}$ sharply decreases when the applied potential increases again. The same behavior was observed for the perpendicular squareness factor $S_{\perp}$, but with a slight increase of $S_{\perp}$ followed by a slight decrease. As the applied potential increases up to V_{Cr}, the squareness factor S ($S_{//}$ and $S_{\perp}$) increases with decreasing mean grain size D. Beyond this critical potential, S and D decrease. In fact, this decrease can be explained by the refinement of the grains size which, in turn, reduces the effective anisotropy constant and reinforce the ferromagnetic exchange coupling [50]. It should be noted that in a previous section (Sect.A.2), we found that the stress (mean grain size) increases (decreases) when the applied potential increases up to V_{Cr}, thus one may relate the increase of S to the increase of stress. While beyond V_{Cr}, the decrease of S may be due to the relaxation of the stresses and also to the increase of the mean grain size. Note that this behavior is similar to the one found in reference [31].

3.3.3. The saturation fields

The behavior of the saturation field H_{sat} makes it possible to distinguish between the hard and easy directions and offers an indication on the magnetic anisotropy. The variation of the saturation field as a function of the applied potential, for both configurations, is shown in Fig. 7. We see that the parallel saturation field $H_{sat//}$ monotonously decreases with increasing applied potential, but with a sharp decrease up to V_{Cr} followed by a slight decrease beyond this critical potential. The same behavior was observed for the perpendicular saturation field $H_{sat\perp}$ in the potential range greater than V_{Cr}. For all samples, except for the sample with -1.8 V, $H_{sat//}$ has the highest values than that of $H_{sat\perp}$. Incidentally, this sample is associated with a low stress and a higher resistivity value (see Table 1). The decrease of H_{sat} with increasing applied potential (decreasing Ni thickness) may indicate a change in the magnetic easy direction, such as from in-plane to out-of plane [35]. This is probably due to the reduction in

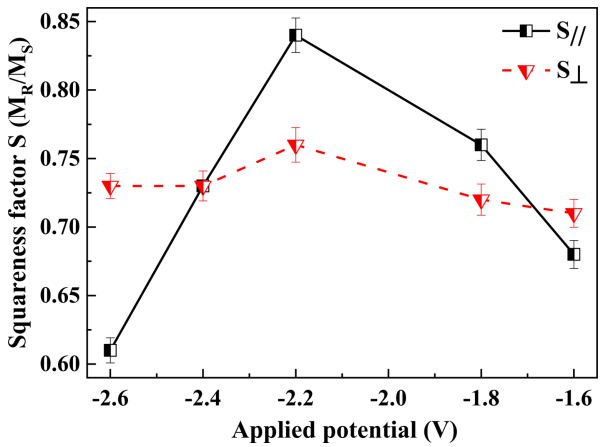

Fig. 6. (Color online) Variation of the squareness factor S vs. applied potential for H parallel and perpendicular to the film plane.

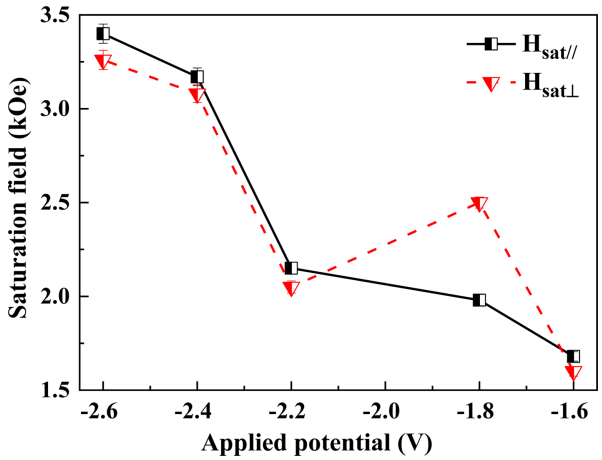

Fig. 7. (Color online) Variation of the saturation field H_{sat} vs. applied potential for H parallel and perpendicular to the film plane.

the in-plane magnetic anisotropy caused by the increasing of effective random magnetic anisotropy which randomizes the orientation of magnetization [51]. Therefore, we conclude this from the H_{sat} behavior along with the shape of the hysteresis curves that the magnetization is in the plane of the films for the considered applied potential (thickness) range. Also, a transition of the easy axis of magnetization from in-plane to out-of-plane with increasing nickel film thickness was found in the literature [52, 53]. Regarding the behavior of the saturation field with grain size D, we found that H_{sat} progressively increases with increasing D.

4. Conclusion

In this present study, we concluded that the variation of the applied potential (from -2.6 to -1.6 V) can be affect the surface morphology, improving the structural and electrical stability, and enhancing magnetic properties of Ni films electrodeposited onto *n*-Si (111) substrate. We found a strong <111> texture confirmed by the high $TC_{(hkl)}$ values of the (111) plane. The mean grain size monotonically decreases with increasing the applied potential. Also, a compressive internal stress on the films was found, the stress increases up to a critical potential V_{Cr}(-2.2 V), then it is relieved. Internal stress can affect the magnetic properties; the parallel coercive field $H_{C//}$ and the squareness factor S ($S_{//}$ and $S_{\perp}$) increases concurrently with increasing internal stress when the applied potential is increased up to V_{Cr}. Beyond the critical potential, stress is relieved and the parallel coercive field and the squarness factor decrease. On the other hand, the variation of H_C with Ni thickness (t) may follow the expected Neel's relation $H_C = At^{-n}$. The observed increase in Hc with D indicates that our findings align with Hoffman's model. All the while, the parallel saturation field H_{sat} monotonously decreases with increasing applied potential. The film electrodeposited at larger applied potential has a higher surface roughness which will be smoother for the lower applied potential. The sheet resistance monotonously increases with an increasing applied potential, simultaneously decreasing Ni thickness and grain size. It should be noted that the electrical resistivity, ρ decreases up to *rms* equal to 12.91 nm (which corresponds toV_{Cr}), then increases as the *rms* is increased further.

References

[1] Z. Zhao, P. Zhu, L. Yang, and Y. Geng, J. Adhes. Sci. Technol. **33**, 301 (2019).
[2] P. Elumalai, H. N. Vasan, M. Verelst, P. Leeante, V. Carles, and P. Taihades, Materials Research Bulletin **37**, 353 (2002).
[3] D. R. Rolison. J. W. Long, J. C. Lytle, A. E. Fischer, C. P. Rhodes, T. M. McEvoy, M. E. Bourg, and A. M. Lubers, Chem. Soc. Rev. **38**, 226 (2009).
[4] L. T. Romankiw and T. A. Palumbo. Electrodeposition Technology, Theory and Practice, Ed. L.T. Romankiw, D.R. Turner, Electrochemical Society, Pennington, NJ (1988) p. 13.
[5] P. C. Searson and T. P. Moffat, Critical Rev. Surf. Chem. **3**, 171 (1994).
[6] M. Hemmous, A. Layadi, A. Guittoum, N. Souami, M. Mebarki, and N. Menni, Thin Solid Films **562**, 229 (2014).
[7] S. Akbulut, A. Akbulut, M. Özdemir, and F. Yildiz, J. Magn. Magn. Mater. **373**, 155 (2015).
[8] M. Sobri, A. Shuhaimi, K. M. Hakim, V. Ganesh, M. H. Mamat, M. Mazwan, S. Najwa, N. Ameera, Y. Yusnizam, and M. Rusop, Superlattice. Microst. **70**, 82 (2014).
[9] J. D. Lee, H. S. Kim, S. Y. Jeong, K. H. Kim, J. J. Lee, and J. E. Kim, Curr. Appl. Phys. **10**, 249 (2010).
[10] J. M. Lee, K. K. Jung, and J. S. Ko, Curr. Appl. Phys. **16**, 261 (2016).
[11] L. Ren, W. Wang, C. Yu, S. Duan, W. Ma, and K. Zhang, Funct. Mater. Lett. **11**, 1850011 (2018).
[12] S. Fazli and M. E. Bahrololoom, Metall. Mater. Trans A **47A**, 4317 (2016).
[13] R. M. Penner, Acc. Chem. Res. **33**, 78 (2000).
[14] H. Wang, R. Liu, W. Q. Jiang, J. Zhu, J. Z. Feng, G. F. Ding, and X. Zhao, Appl. Surf. Sci. **257**, 2203 (2011).
[15] X. Yu and Z. Yuan, Metall. Mater. Trans. B **50B**, 587 (2019).
[16] F. Yang, X.-F. Zhang, H. Yang, Y.-N. Liu, S.-J. Hao, and L.-S. Cui, Trans. Nonferrous Met. Soc. China **29**, 424 (2019).
[17] P. Hasanpour, P. Salehikahrizsangi, K. Raeissia, M. Santamaria, L. Calabrese, and E. Proverbio, Surf. Coat. Tech. **368**, 147 (2019).
[18] I. Bakonyi, V. A. Isnaini, T. Kolonits, Z. S. Czigány, J. Gubicza, L. K. Varga, E.-T Kádár, L. Pogány, L. Péter, and H. Ebert, Philos. Mag. **99**, 1139 (2019).
[19] G.-R. Wang, P.-S. Hung, S.-Y Chang, J.-M. Yang, Y.-C. Tseng, and P.-W. Wu, J. Electrochem. Soc. **167**, 022505 (2020).
[20] A. Góral, T. Czeppe, and K. Berent, Surf. Coat. Tech. **369**, 95 (2019).
[21] N. Mansouri, N. Benbrahim-Cherief, E. Chainet, F. Charlot, T. Encinas, S. Boudinar, B. Benfedda, L. Hamadou, and A. Kadri, J. Magn. Magn. Mater. **493**, 165746 (2020).
[22] F. Nasirpouri, H. Cheshideh, A. Yu. Samardak, A.-V. Ognev, A.-A. Zubkov, and A.-S. Samardak, Ceram. Int. **45**, 11258 (2019).
[23] X. Yu, M. Wang, Z. Wang, X. Gong, and Z. Guo, Appl. Surf. Sci. **360**, 502 (2016).

[24] A. C. Mishra, A. K. Thakur, and V. Srinivas, J. Mater. Sci. **44**, 3520 (2009).
[25] M. Boubatra, A. Azizi, G. Schmerber, and A. Dinia, Ionics **18**, 425 (2012).
[26] N. P. Wasekar, P. Haridoss, S. K. Seshadri, and G. Sundararajan, Surf. Coat. Tech. **291**, 130 (2016).
[27] L. Shen, M. Xu, W. Jiang, M. Qiu, M. Fan, G. Ji, and Z. Tian, Appl. Surf. Sci. **489**, 25 (2019).
[28] Z. Rao, S. J. Hearne, and E. Chason, J. Electrochem. Soc. **166**, D3212 (2019).
[29] F. Nasirpouri, M. R. Sanaeian, A. S. Samardak, E. V. Sukovatitsina, A. V. Ognev, L. A. Chebotkevich, M.-G. Hosseini, and M. Abdolmaleki, Appl. Surf. Sci. **292**, 795 (2014).
[30] P. Evans, C. Scheck, R. Schad, and G. Zangari, J. Magn. Magn. Mater. **260**, 467 (2003).
[31] M. Hemmous, A. Layadi, L. Kerkache, N. Tiercelin, V. Preobrazhensky, and P. Pernod, Metall. Mater. Trans A. **46a**, 4143 (2015).
[32] M. Lukaczynska, E.-A. MernissiCherigui, A. Ceglia, K.-V. Den Bergh, J.-D. Strycker, H. Terryn, and J. Ustarroz, Electrochim. Acta **319**, 690 (2019).
[33] G. Gubbiotti, G. Carlotti, S. Tacchi, Y.-K. Liu, C. Scheck, and R. Schad, and G. Zangari, J. Appl. Phys. **97**, 10J102 (2005).
[34] S. Hope, J. Lee, P. Rosenbusch, G. Lauhoff, J. A. C. Bland, A. Ercole, D. Bucknall, J. Penfold, H. J. Lauter, V. Lauter, and R. Cubitt, Phys. Rev. B **55**, 11422 (1997).
[35] J. Gong, S. Riemer, M. Kautzky, and I. Tabakovic, J. Magn. Magn. Mater. **398**, 64 (2016).
[36] N. Boussaa, A. Guittoum, and S. Tobbeche, Vacuum **77**, 125 (2005).
[37] L. Lutterotti, MAUD CPD Newsletter (IUCr) **24**, 2000.
[38] H. E. Swanson, and E. Tatge, Natl. Bur. Stand. (U.S.), Circ. 539. **I**, 13 (1953).
[39] A. Shumskaya, V. Bundyukova, A. Kozlovskiy, M. Zdorovets, K. Kadyrzhanov, G. Kalkabay, and E. Kaniukov, J. Magn. Magn. Mater. **497**, 165913 (2020).
[40] T. Kacel, A. Guittoum, M. Hemmous, E. Dirican, R. M. Öksüzoglu, A. Azizi, A. Laggoun, and M. Zergoug, Surf. Rev. Let. **25**, 1850058 (2017).
[41] D. A. Porter and K. E. Easterling, Phase Transformations in Metals and Alloys, Chapman & Hall, London (1992) p. 115.
[42] T. Emoto, K. Akimoto, A. Ichimiya, and K. Hirose, Appl. Surf. Sci. **190**, 113 (2002).
[43] D. G. Fink and D. Christiansen, Electronics Engineers' Handbook, 3rd, McGraw-Hill, New York, USA (1989) p. 237.
[44] Y. Tang, D. Zhao, D. Shen, J. Zhang, B. Li, Y. Lu, and X. Fan, Thin Solid Films **516**, 2094 (2008).
[45] J. G. Kim, K. H. Han, S. H. Song, and A. Reilly, Thin Solid Films **440**, 54 (2003).
[46] H. Hoffmann and T. Fujii, J. Magn. Magn. Mater. **128**, 395 (1993).
[47] F. Kneller and F. E. Luborsky, J. Appl. Phys. **34**, 656 (1963).
[48] B. D. Cullity, Introduction to Magnetic Materials, Addison-Wesley, Massachusetts (1972) pp. 359-408.
[49] L. Kerkache, A. Layadi, M. Hemmous, A. Guittoum, M. Mebarki, N. Tiercelin, A. Klimov, V. Preobrazhensky, and P. Pernod, SPIN **9**, 1950006 (2019).
[50] Y.-T. Chen, J.-Y. Tseng, T.-S. Sheu, Y. C. Lin, and S. H. Lin, Thin Solid Films **544**, 602 (2013).
[51] P. Ravikumar, D. Taparia, and P. Alagarsamy, J. Supercond. Nov. Magn. **31**, 3761 (2018).
[52] M. Farle, B. Mirwald-Schulz, A. N. Anisimov, W. Platow, and K. Baberschke, Phys. Rev. B **55**, 3708 (1997).
[53] K. Baberschke and M. Farle, J. Appl. Phys. **81**, 5038 (1997).